LASER & PHOTONICS REVIEWS
www.lpr-journal.org

Quad-SPIM: A High-Speed, Multi-Color Light-Sheet Microscope for 3D Imaging of Large Cleared Human Brain Tissues

Laura Perego, Franco Cheli, Samuel Bradley, Danila Di Meo, Luca Giannoni, Josephine Ramazzotti, Federica Fenizi Caria, Giuseppe Sancataldo, Michele Sorelli, Giacomo Mazzamuto, Irene Costantini, and Francesco Saverio Pavone*

Light-sheet fluorescence microscopy (LSFM) is a powerful tool for high-resolution volumetric imaging of biological samples, offering fast acquisition speeds and reduced photodamage. However, its application to large, optically cleared human tissues—such as postmortem brain specimens—remains technically challenging due to constraints in speed, resolution, spectral flexibility, and sample handling. In this work, a custom-built, high-speed, multi-color LSFM system specifically designed for large-scale imaging of cleared human brain tissue with subcellular resolution is presented. The system enables simultaneous four-channel acquisition and achieves imaging speeds exceeding 3 cm^3 h^{-1}, thanks to a custom optical design and an optimized software for data handling. The platform features a large and stable imaging chamber with precise sample positioning, and an optimized detection path that provides four-channel imaging, avoiding cross-talk and preserving image quality across extended fields of view. The capabilities and performance of the microscope by imaging postmortem, optically cleared human brain samples, revealing cytoarchitectonic and vascular features across centimeter-scale volumes are demonstrated. This LSFM platform provides a robust and scalable solution for high-throughput imaging of large human tissues, with potential applications in neuroanatomy, connectomics, and neuropathology.

1. Introduction

Visualizing and quantifying biological processes in living organisms, tissues, and cells requires microscopy techniques that are gentle with the specimen, yet provide fast, high-resolution 3D imaging across large fields of view (FOVs). Traditional fluorescence microscopy approaches-such as widefield fluorescence microscopy (WFM)[1–5] and laser scanning confocal microscopy (LSCM)[6,7]-have long been employed to investigate biological samples at cellular and subcellular resolution, enabling accurate structural and functional analysis. In WFM, the entire sample volume is illuminated, and fluorescence is collected by a two-dimensional detector. While this enables rapid acquisition, the contrast is often reduced due to the presence of out-of-focus fluorescence, which is collected from regions above and below the focal plane. In contrast, LSCM overcomes this by sequentially scanning a tightly focused excitation beam and rejecting out-of-focus signal by means of a confocal pinhole, thereby

L. Perego, F. Cheli, S. Bradley, D. Di Meo, J. Ramazzotti, F. F. Caria, M. Sorelli, G. Mazzamuto, I. Costantini, F. S. Pavone
European Laboratory for Non-Linear Spectroscopy (LENS)
University of Florence
Sesto Fiorentino 50019, Italy
E-mail: peregol@lens.unifi.it

The ORCID identification number(s) for the author(s) of this article can be found under https://doi.org/10.1002/lpor.202501725

DOI: 10.1002/lpor.202501725

S. Bradley, G. Mazzamuto, F. S. Pavone
Department of Physics and Astronomy
University of Florence
Sesto Fiorentino 50019, Italy

D. Di Meo, I. Costantini
Department of Biology
University of Florence
Sesto Fiorentino 50019, Italy

L. Giannoni
Department of Medical Physics and Biomedical Engineering
University College London
London WC1E 6BT, UK

G. Sancataldo
Department of Physics and Chemistry
University of Palermo
Palermo 90128, Italy

generating optical sectioning with improved axial resolution. However, this point-scanning approach is inherently slow and unsuitable for large volumetric datasets or long-term imaging, as it also leads to significant photobleaching and phototoxicity.[8]

To address these limitations, over the past two decades, the field of optical imaging has witnessed the emergence of new approaches capable of delivering fast, gentle, and volumetric imaging. Among these, light-sheet fluorescence microscopy (LSFM) has rapidly become a leading technique for high-resolution, high-throughput imaging of biological systems. LSFM has emerged as a valuable solution among the available fluorescence microscopy techniques thanks to its ability to image biological systems for long periods of time with reduced photodamage to the specimen, while providing fast, 3D information with high spatiotemporal resolution over large FOVs.[9] LSFM achieves optical sectioning by illuminating only a thin plane of the specimen with a laminar sheet of light and collecting the emitted fluorescence orthogonally. This geometry not only limits photodamage to the illuminated plane, but also enables rapid acquisition of entire sample planes without the need for raster scanning or confocal apertures. As a result, LSFM drastically improves imaging speed and viability for long-term studies, making it particularly advantageous for dynamic and large-scale biological imaging.[10,11]

Since its introduction, LSFM has transformed biological research, proving especially effective across a wide range of scientific fields, including cell biology,[12] developmental biology,[13] histopathology[14] and neuroscience,[15] among others. In neuroscience, LSFM has enabled the detailed mapping of neural circuitry and brain activity in living animals[12] and fixed samples,[16] as well as studies on the reconstruction of the brain vasculature.[17] Crucially, animal and human cleared brain tissue can be studied at sub-micron resolution, revealing new insights into the brain cytoarchitecture, connectivity, and neuropathological features associated with critical diseases affecting the nervous system.[18–25]

As this technique continues to evolve, ongoing developments aim to push the boundaries of resolution, imaging depth penetration, and spectral multiplexing, in order to broaden its potential applications. A key challenge lies in imaging large or densely packed specimens, where light scattering and absorption may severely degrade image quality. Indeed, LSFM requires biological samples to be optically transparent to light to enable their volumetric reconstruction.[26–28] Advancements in multiphoton excitation and non-linear optics hold promise for overcoming these limitations.[29] Furthermore, integrating LSFM with other modalities, such as magnetic resonance imaging (MRI), positron emission tomography (PET), polarized light imaging (PLI), and optical coherence tomography (OCT) can offer a multimodal approach for anatomical and functional investigations.[22,30–32]

Another critical challenge in light-sheet microscopy is achieving simultaneous high resolution, large FOVs, and short acquisition times, particularly when imaging complex human tissues with multiple fluorophores. Many available LSFM systems face trade-offs between these parameters.[2,33–38]

In this work, we present an innovative custom-built, high-speed, multi-wavelength light-sheet fluorescence microscope optimized for fast volumetric imaging of large optically cleared human brain tissues. The system is capable of simultaneous four-channel imaging with micrometer resolution at exceptionally high imaging speed across centimeter-scale volumes. It combines a novel optical design, rapid volumetric acquisition, and custom software for automated image acquisition and processing.[39] After a complete characterization of the technical features of the system, we demonstrate its utility by performing structural imaging of human brain cortical and subcortical regions, capturing detailed neuroanatomical and vascular features. This platform represents a robust and accessible tool for large-scale human brain imaging and offers new opportunities in neuropathology, neuroanatomy, and connectomics studies.

2. Results

2.1. LSFM Microscope Design and Construction

The proposed Light Sheet Fluorescence Microscope (LSFM) is equipped with four different laser sources enabling fast imaging of human brain tissues in four colors. A schematic of the apparatus is shown in **Figure 1a**. The system is capable of performing simultaneous imaging of up to four differently labeled markers with sensitivity down to the single cell. The four selected laser lines consist of four diode-pumped solid-state lasers (Figure 1a). In particular, from left to right, a Cobolt 06-MLD 488 nm laser, with a maximum output power $P_{max} = 100$ mW, a Cobolt 06-DPL 561 nm laser with $P_{max} = 100$ mW, a Cobolt 04 series 594 nm laser with $P_{max} = 50$ mW, and finally a Cobolt 06-MLD 647 nm laser with $P_{max} = 130$ mW. The collimated beam waist of the four lasers is $\omega = (0.70 \pm 0.05)$ mm after 1:4 expansion through a system of telescopes positioned in front of the laser output. The four laser lines are combined into a single collimated beam and directed toward the Acousto-Optic Tunable Filter (AOTFnC-400.650-TN, AA Opto-Electronics) by means of three long-pass dichroic mirrors (FF552- Di02, FF596-Di01, and FF649-Di01, all of them manufactured by Semrock). A half-wave plate is placed in front of each laser head to finely adjust the beam polarization, thus optimizing the power output of the first-order diffracted beam exiting the AOTF, and two irises are positioned at a reciprocal distance of 30 cm to function as a reference for fine alignment of the collimated beam before entering the AOTF. The AOTF is used for selection and blanking of the desired laser lines. After the AOTF, the four combined beams are directed toward the diffraction prism (GK7 glass, Thorlabs), which separates the four colors again, with an angular deviation determined by Snell's law. In this way, four slightly separated beams reach the galvanometric mirror (Galvo set, 8320K, Cambridge Technology), which will thus generate four digitally scanned light sheets. The galvo scanner is placed at a distance of 200 mm from an achromatic doublet (VIS AR coating, Thorlabs, f = 200 mm), which is used as the scanning lens. By placing the galvanometric mirror at a distance matching the focal length of the scanning lens, the rotations of the galvo scanner are converted into linear displacements

M. Sorelli
Department of Information Engineering
University of Florence
Florence 50139, Italy
G. Mazzamuto, F. S. Pavone
National Research Council – National Institute of Optics (CNR-INO)
Sesto Fiorentino 50019, Italy

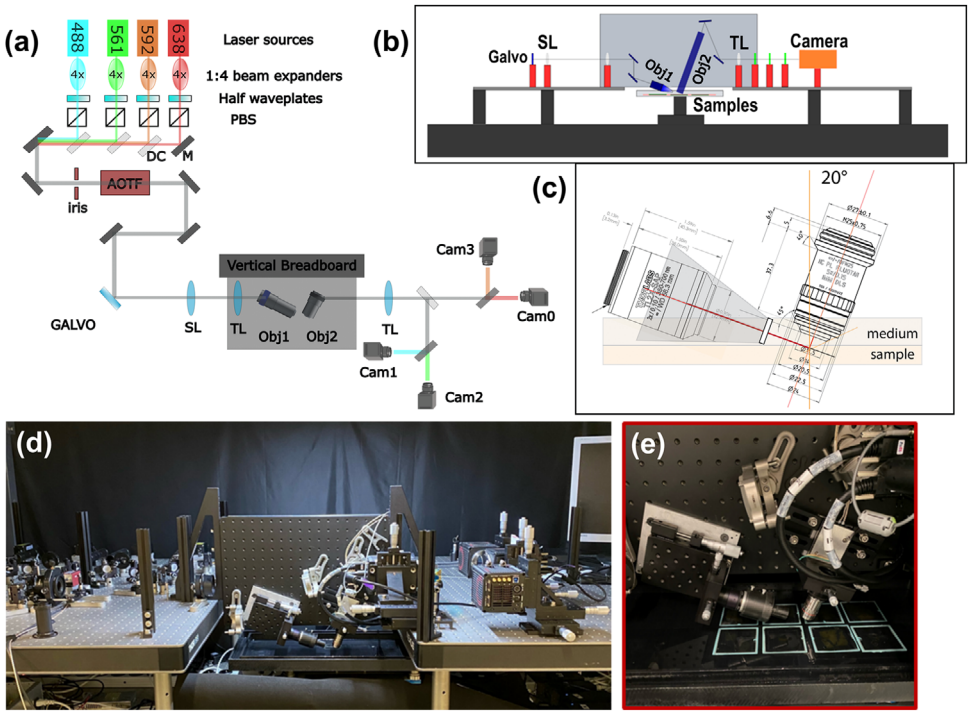

Figure 1. a) Schematic representation of the optical path of our LSFM setup. For simplification, the beam combining the 4 laser lines is depicted in grey. PBS: polarizing beam splitter; DC: dichroic mirrors; SL: scanning lens, TL: tube lens. b) Frontal view scheme: the two lifted lateral breadboards hold the vertical breadboards where the objectives are located. c) Graphical representation of the positions of the excitation and detection objectives, which are tilted by 20 degrees relative to the horizontal and vertical axes, respectively. d) Photo of the portion of the setup which includes the vertical breadboard and the custom-made sample chamber. e) Detail of the sample chamber where up to 8 different specimens can be accommodated.

of the four beams on the back focal plane of the illumination objective (TL2X-SAP, Thorlabs, 2X/0.10 Numerical Aperture (NA), 56.3 mm working distance), which in turn creates the four digitally scanned light sheets. The galvanometric mirror rotations are controlled by means of a multifunction I/O board from National Instruments, which allows the user to select the scanning rate and the angular rotation of the mirror.

The detection part of the setup is built around the detection objective, a Leica HC PL Fluotar 5X/0.15 NA immersion objective with a working distance of 4.8 mm. This objective is designed to be used with high-RI immersion media, such as BABB, 2.2'-thiodiethanol (TDE), or glycerol, and includes appropriate optical correction for such environments, avoiding the rise of possible spherical aberrations. Our samples are mainly human tissues cleared with the SHORT method, as described in the Experimental Section, which is based on the usage of TDE as the clearing agent. TDE can lead to potential respiratory irritation if inhaled for long periods of time, which is the case with long imaging sessions. For this reason, we adopt glycerol (91% v/v) as our imaging medium, since it matches the refractive index (RI) of TDE and presents lower toxicity. In particular, the sample is positioned between two quartz glass slides, which have the same RI of glycerol (91% v/v) and TDE, in a sandwich configuration, and the space between the two glasses is filled with TDE. The two glass slides are then glued together to prevent TDE and glycerol mixing, enabling the performance of the experiments by using glycerol as the imaging medium. This detection objective was chosen since it was, to our knowledge, the best commercially accessible solution available in reasonable times that met our requirements of 5× magnification, large FOV, long working distance, and glycerol-compatible immersion detection objective. In future works, we plan to buy and integrate custom-built objective lenses with higher NA and longer working distances to further improve the system resolution and to limit space constraints.

Both the illumination and detection objectives are placed on a vertical breadboard and mounted on XY translation mounts with micrometric screws, which permit the XY movement of the objective in a 6 mm-travel range (ST1XY-S, Thorlabs). For movements on the Z plane, the illumination objective is mounted on a 25-mm travel manual stage (XNR25P/M, Thorlabs), whereas the detection objective is fixed on a 25-mm travel motorized stage (M-112.2DG1, Physik Instrumente). The illumination objective is tilted by 20 degrees relative to the horizontal plane, whereas the detection objective is oriented at an angle of 110 degrees, considering the same reference system, thus resulting in the perpendicular mutual orientation of the two objectives (Figure 1c,e). This unconventional orientation of the objectives with respect to the sample plane is necessary due to physical space constraints. In particular, the relatively limited free working distance of the detection objective requires a smaller angle of incidence for the illumination arm to avoid mechanical interference while imaging the whole sample thickness. If these objectives are changed in the future with new ad-hoc designed items, a possible transition to the more classical and symmetrical 45 degrees inverted configuration will be taken into account, as it would lead to an easier implementation and alignment of the setup.

The vertical breadboard is hung between the two horizontal optical platforms to allow the two objectives to move freely upon the sample holder (Figure 1b,d). After the detection objective, a 75-mm diameter achromatic doublet (f = 200 mm, Edmund Optics) is used as the objective tube lens. Finally, three dichroic filters (Ultra Series Dichroic Filters, Alluxa) with cut-off frequencies of 520, 581, and 604 nm are mounted to split the image into four channels, separately acquired by dedicated scientifica Complementary Metal-Oxide-Semiconductor (sCMOS) cameras (Orca Flash 4 v.3, Hamamatsu). Each camera is placed at a distance of 200 mm from the tube lens for a correct focusing of the image, and each of them is mounted on a three-axis manual stage (PT3/M, Thorlabs) to precisely adjust its position. Band-pass filters (Chroma, ET576/31m, ET576/31m, AT625/30m, ET690/50m) are positioned in front of each camera to avoid cross-talking between channels.

A custom specimen holder was designed and manufactured ad hoc for the microscope: a block of Polyvinyl Chloride (PVC) was grooved to a depth of 20 mm, leaving 20 mm-high edges to create a chamber to contain the imaging medium. Eight 62 × 62 mm squared slots were carved on the bottom surface of the chamber in order to allocate up to eight 60 × 60 mm glass slides containing the samples to be imaged (Figure 1e). A hole was drilled at the bottom of the chamber to incorporate a drainage system for the imaging medium through a dedicated tap.

The whole imaging chamber is mounted on motorized stages for sample scanning. In particular, the movement on the XY plane is accomplished through a precision linear stage with 300-mm travel range (M-531.PD, Physik Instrumente), and on top of this stage, a 26-mm travel vertical precision stage (L-310, Physik Instrumente) is assembled to move the chamber along the vertical direction. To accommodate this range of motion, avoiding mechanical obstructions, and to allow the objectives to move freely for fine focusing and clear access to the sample volume, the vertical breadboard must be suspended between the two raised platforms parallel to the sample plane, with the left side dedicated to the illumination pathway and the right side hosting the detection optics. Importantly, the system is entirely built on a single optical table, and a modular architecture is then developed around the sample place with the aid of a vertical breadboard and two optical platforms, as shown in the scheme of Figure 1b.

This design offers a practical balance between optical accessibility, mechanical stability, and ease of the alignment, but we believe that users with different space constraints could reproduce this system with minor adaptations, tailoring it to their specific needs.

2.1.1. System Characterization

The newly built LSFM microscope was fully characterized in terms of resolution, signal-to-noise (SNR), and signal-to-background (SBR) ratios. Both lateral and axial resolution of the setup were determined by evaluating the point spread function (PSF) of the optical system. For a correct measurement, samples with fluorescent beads were prepared (Figure S1a, Supporting Information) as described in the Materials and Methods section. The sample was excited with each laser line and imaged in the four channels for a thorough assessment of the PSF. After imaging, the intensity profiles (N = 15 for each channel) were projected along the three X, Y, and Z axes of the beads. A Gaussian fitting was performed for each bead axis, and the corresponding full width at half maximum (FWHM), which can be considered equal to the size of the PSF, was evaluated (Figure S1b, Supporting Information). Results are reported in **Table 1**.

For a correct evaluation of the SBR and the SNR, a 3D reconstruction of a slab of human brain tissue from Broca's area was acquired (Figure S2, Supporting Information). The tissue was stained with the Neuronal Nuclei (NeuN) primary antibody and the Alexa Fluor 647 secondary antibody according to the protocol described in the Experimental Section. The mean fluorescence signal (μ_s) was estimated from 100 regions of interest (ROIs), whereas 10 ROIs were taken into consideration for evaluating the background mean intensity (μ_b). The SNR was calculated from the same ROIs adopted for the SBR. The mean SBR and SNR calculated are reported in Equations (1) and (2).

$$SBR = \frac{\mu_s}{\mu_b} = 1.7 \pm 0.1 \tag{1}$$

$$SNR = \frac{\mu_s - \mu_b}{\sigma_b} = 11.5 \pm 0.2 \tag{2}$$

The presented results show the capability of the system to achieve a lateral resolution ranging between 2.1 and 2.7 µm, enabling the visualization of individual neurons at single-cell resolution. The primary limitation arises in the axial resolution when imaging thick specimens, such as those with a depth of 1 mm or more. To accommodate the full FOV, the confocal parameter of the illumination beam must be matched accordingly, which constrains the minimum achievable light-sheet thickness. However, for thinner samples (i.e., <1 mm), the light-sheet thickness can be reduced by increasing the beam diameter at the back focal aperture of the illumination objective. This is achievable through the integration of a beam expander with a suitable magnification factor in front of each laser source output, though this comes at the cost of a reduced confocal parameter and FOV. Quantitative assessments of SBR and SNR indicate values compatible with robust image analysis workflows for the extraction of biologically meaningful information. Nonetheless, maintaining high SBR remains challenging, particularly when imaging tissues with pronounced autofluorescence or when using fluorophores with low specificity or quantum yields. Therefore, careful optimization of sample preparation protocols is essential to minimize such effects and ensure optimal imaging conditions.

2.2. Multiplexing and Simultaneous 4-Channel Acquisition

After the microscope characterization, a first sample was acquired following the pipeline graphically depicted in **Figure 2a**, in order to prove the ability of the quad-SPIM system to perform simultaneous acquisitions in 4 different emission channels without cross-talking or other problems related to multiplexing. The sample consisted of a human Broca's area slab measuring (52 × 35 × 0.5 mm), which was cleared with the SHORT protocol[40] as described in the Experimental Section and stained with YOYO-1, Somatostatin (SST), Thyroxine Hydroxylase (TH),

Table 1. PSF of 500-nm-diameter fluorescent spheres. N = 15 for each axis in each channel. Measurements from each channel and each axis were averaged to obtain the final values, which, together with their standard deviation, define the resolution of the microscope.

Excitation wavelength [nm]	PSF_x^{teo} [µm]	PSF_y^{teo} [µm]	PSF_z^{teo} [µm]	PSF_x^{exp} [µm]	PSF_y^{exp} [µm]	PSF_z^{exp} [µm]
488	1.7	1.7	4.3	2.1 ± 0.3	2.2 ± 0.4	7.2 ± 1.5
561	2.0	2.0	4.9	2.1 ± 0.1	2.2 ± 0.5	7.6 ± 1.9
594	2.0	2.0	5.3	2.2 ± 0.6	2.5 ± 0.4	7.8 ± 2.2
638	2.2	2.2	5.7	2.1 ± 0.2	2.7 ± 0.3	7.9 ± 0.9

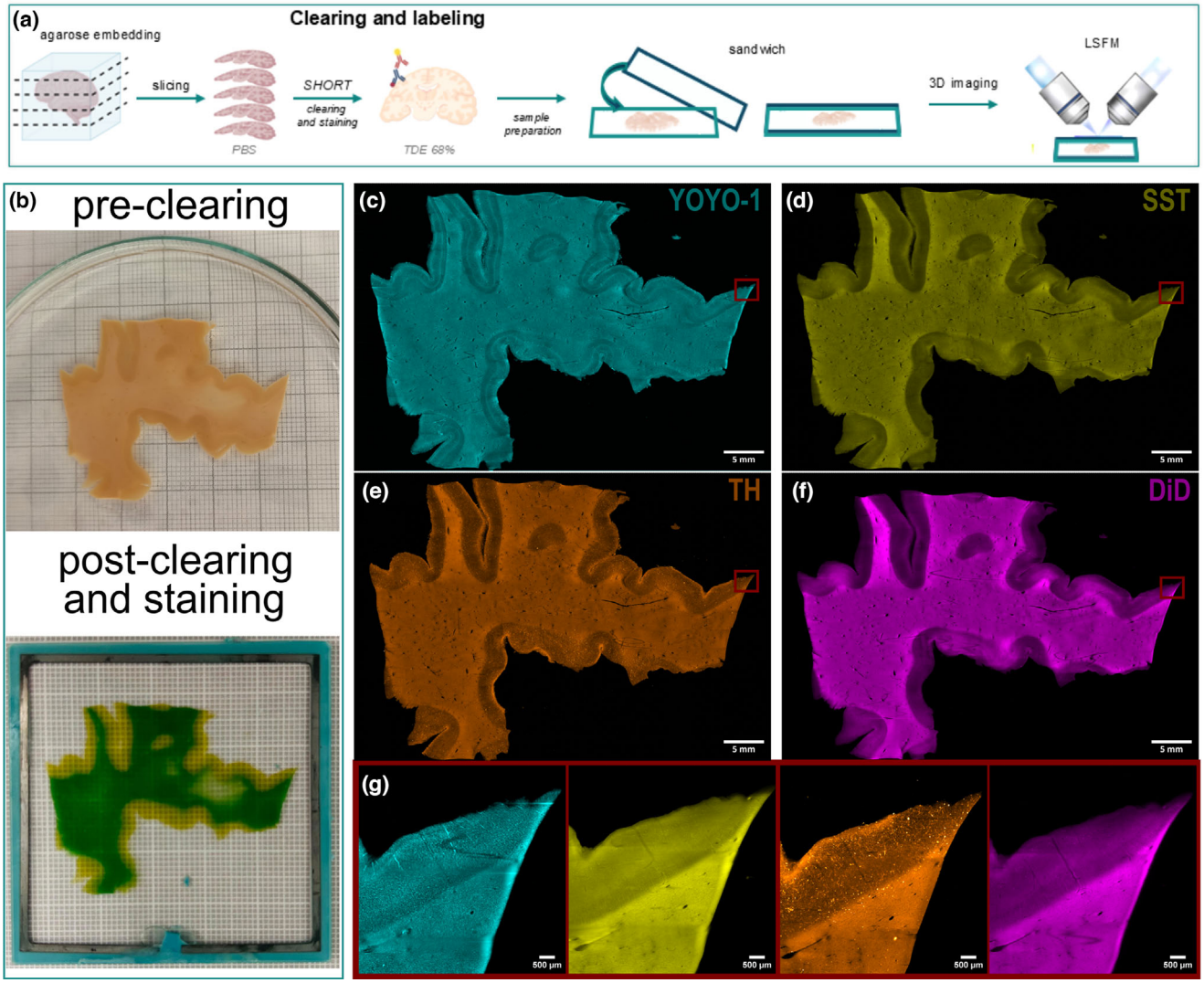

Figure 2. a) Experimental pipeline: clearing and labelling of deparaffinized slabs[25] with the SHORT tissue transformation method, followed by sample preparation in glass sandwich holders and 3D volumetric imaging through LSFM b) Photos of Broca's slab before clearing and after clearing with the SHORT protocols and subsequent staining. Maximum intensity projections of a slab of the human brain's Broca's area imaged with the newly built LSFM setup through simultaneous 4-channel acquisition. The slab is stained with YOYO-1 c), Somatostatin d), Thyroxine Hydroxylase e), and DiD f). Zoomed-in views of the four channels are shown in g).

and DiD, which have excitation peaks respectively at 488, 561, 594, and 647 nm and are employed respectively for the labelling of all nuclei, somatostatinergic and noradrenergic neurons, and all myelinated fibers. Before acquisition, the microscope's ability to image four emission channels simultaneously without cross-talk was tested by switching on one laser at a time and consistently checking that the relative fluorescence emission was visible only in the dedicated camera, thus confirming that no tail of the emission peaks extended into another emission channel and that there was no spectral overlap. After that, the sample was suc-

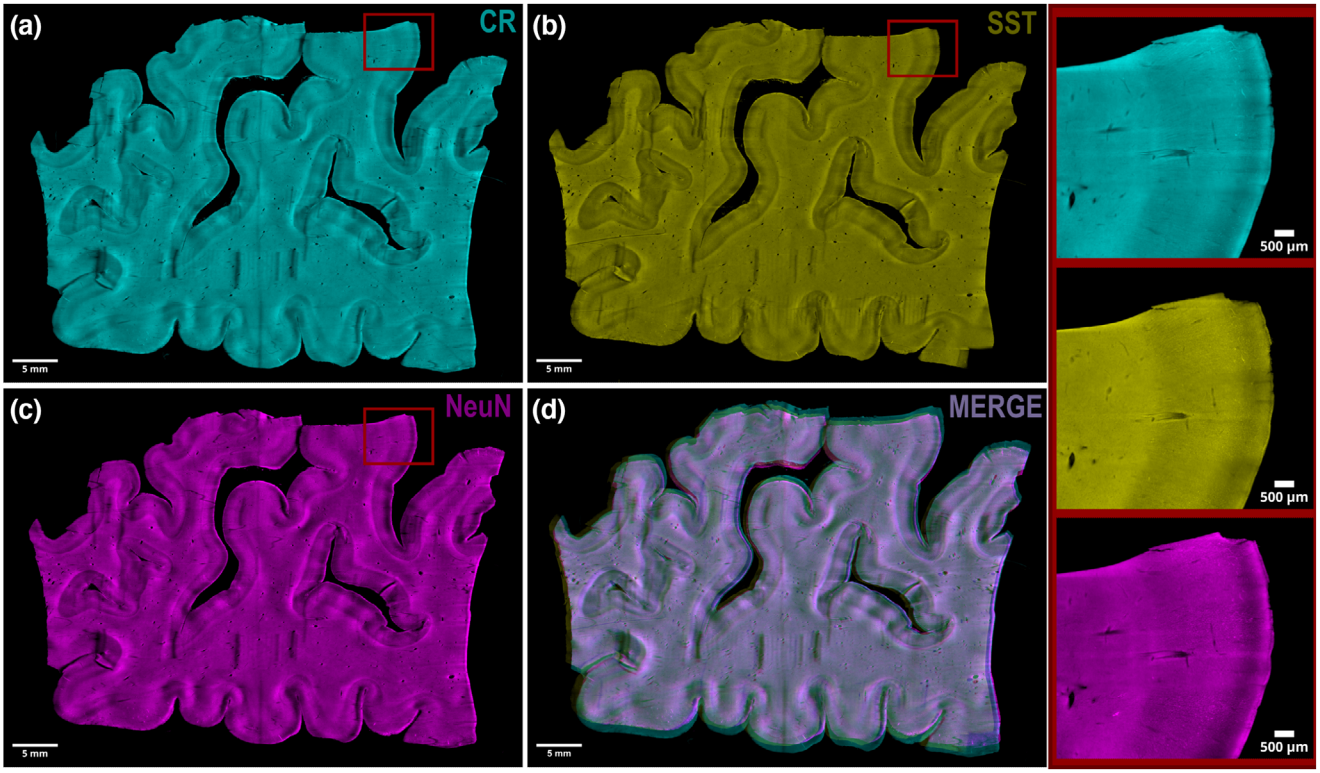

Figure 3. Maximum intensity projection of 3-channel acquisitions of a Broca's area slab measuring 55 × 45 × 0.5 mm. The sample was stained with Carletinin a), Somatostatin b), and NeuN c) primary antibodies. The projection in d) represents a three-channel merged image. The three insets on the right are zoom-in views of the squared region in the three channels.

cessfully acquired by simultaneous illumination with four laser lines and acquisition in the four separated emission channels, thus proving the ability of the system to perform multiplexed measurements. Figure 2 shows the experimental pipeline (a), the sample before and after clearing and staining (b), the maximum intensity projections of the slab in the 4 channels (c,d,e,f), and zoomed regions of the samples to better visualize the staining of different features (g).

2.3. High-Speed Imaging of Large Samples

In order to test the ability of the quad-SPIM to image large samples at high acquisition speeds, we performed imaging of a large human Broca area slab measuring 55 × 45 × 0.5 mm. The sample was cleared with the SHORT protocol as described in the Experimental Section and was labeled with antibodies against different populations of neurons: Calretinin (CR), Somatostatin (SST), and NeuN primary antibodies, to be illuminated with three laser lines (488, 561, and 647 nm). The acquired images were processed to obtain a final 3D stack and a maximum intensity projection (MIP) image for each channel, the latter shown in **Figure 3**. The acquisition was performed by illuminating the sample with the three laser lines simultaneously and with an exposure time of 1 ms. The entire 3D, 3-color acquisition was performed in 47 min and 11 s.

This result confirms the capability of the microscope to rapidly image large-scale samples, thereby fulfilling the specifications for which it was originally designed and built and the intended applications. The system is, in fact, characterized by an imaging speed of 3.2 $cm^3\ h^{-1}$ which, compared to the 0.29 $cm^3\ h^{-1}$ achieved by the dual- selective plane imaging microscope (dual-SPIM) setup already in use in our laboratories,[22] represents an 11-fold improvement in the acquisition speed of biological samples.

2.4. Fiber Orientation Dispersion Comparison

To evaluate the performance of the newly built imaging system in terms of quantitative analysis, a slab from human brainstem tissue was processed and stained with the lipophilic dye DiD for myelinated fiber staining, as described in the Experimental section. The chosen slab was previously imaged with the dual-view, inverted LSFM setup[22,40] to analyze the orientation of fiber bundles. The dual-SPIM microscope is composed of two high-aperture objectives that are tilted by 45° with respect to the sample plane and are positioned orthogonally to each other, alternatively playing excitation and detection roles. This setup has a native resolution of 0.55 × 0.55 × 3.3 µm, thus exceeding the one of the new quad-SPIM system, which has a measured resolution of 2.1 × 2.7 × 7.9 µm when illumination is performed with the 647 nm laser line. The brainstem slab was imaged with both microscopes, and the acquired images were processed as described in the Experimental Section (**Figure 4a,b**). Fiber analysis was performed using an advanced spatial orientation analysis tool, named Foa3D.[41,42] Foa3D enables the automated assess-

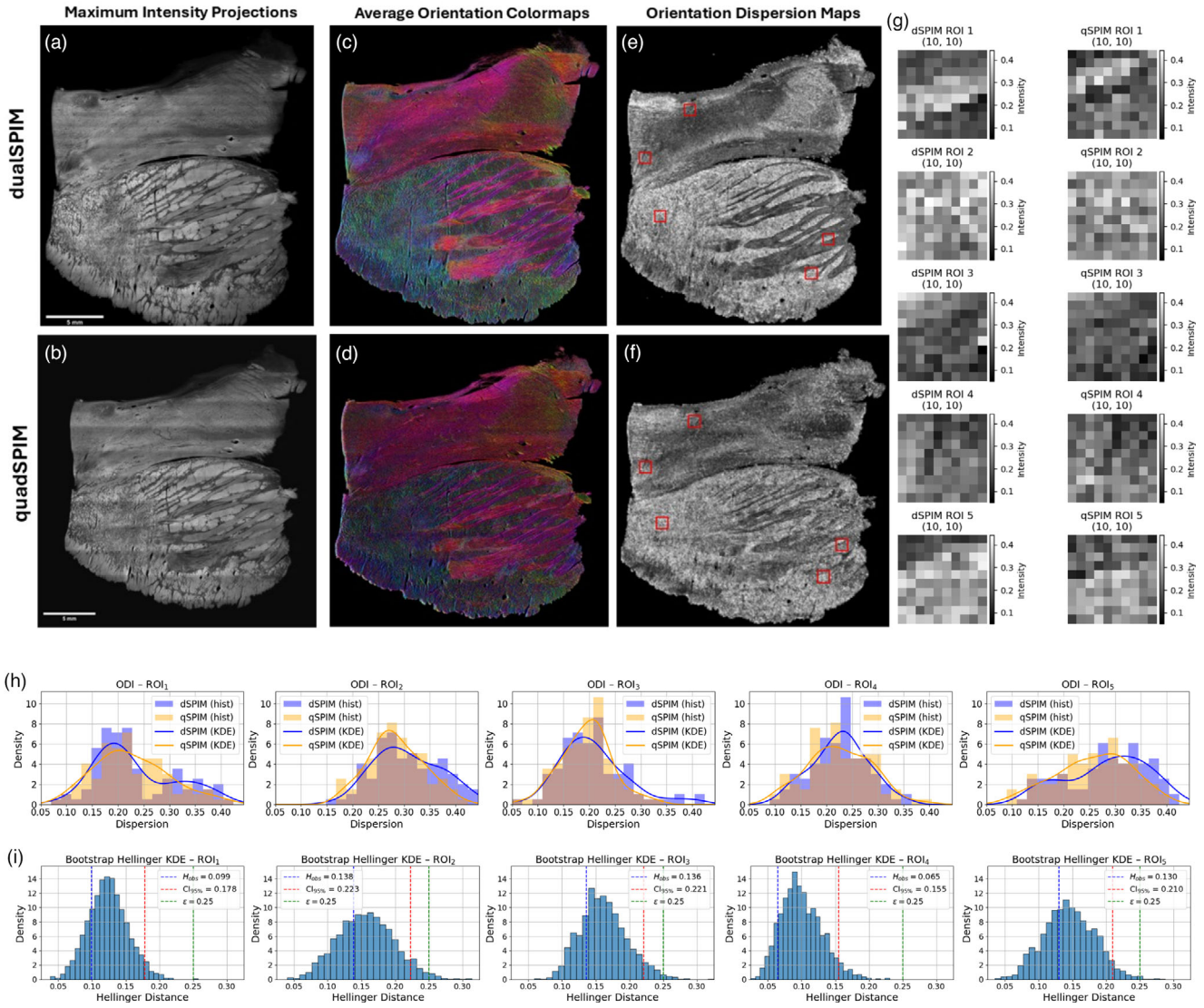

Figure 4. a,b) Maximum intensity projections of the same brainstem slab acquired with dual-SPIM (a) and quad-SPIM (b). Scale bar 5 mm. c,d) Average intensity projections of the 3D fiber orientation colormaps generated by applying Foa3D to the mesoscopic reconstructions of the brainstem slices acquired with the dual-SPIM (c) and quad-SPIM (d) microscopes. e,f) Orientation dispersion maps of myelinated fibers (isotropic pixel size: 100 µm). Red squares are the 5 ROIs selected to test the equivalence. g) Zoomed visualization of the 5 pairs of ROIs extracted from the dual-SPIM (left) and quad-SPIM (right) acquisitions. ROIs are 10 × 10 pixel = 1 mm^2. h) Graphical visualization of dispersion distributions, both with histograms and KDE overlaid Gaussian functions. This combined view provides an intuitive comparison between dual-SPIM (dSPIM) and quad-SPIM (qSPIM) acquisitions, highlighting the central tendency, the overall shape, and the overlap of distributions. i) Visual representation of the Hellinger distribution: the blue line corresponds to the value of the calculated bootstrap Hellinger distance, the red line is the upper boundary of the 95% confidence interval, and the green line is the threshold value of $\epsilon = 0.25$ chosen for the equivalence test.

ment of fiber orientations by employing unsupervised 3D multi-scale Frangi filters, producing multiscale maps of orientation distribution functions and local orientation dispersion (Figure 4c–f). These outputs support accurate quantitative characterization of white matter bundle directionality and facilitate the extrapolation of mesoscopic structural features from orientation details resolved at the native micrometric scale of the LSFM system.

Specifically, Foa3D computes a normalized index of fiber orientation dispersion (ODI), which is quantified, as described below, using the eigenvalues of the local orientation tensor. This tensor is derived from the sum of the outer products of 3D fiber orientations within a super-voxel of a given size, capturing the relationship between local dominant orientations at the corresponding spatial scale:

$$ODI = 1 - \frac{2}{\pi} \cdot \arctan\left(\frac{\lambda_3}{\sqrt{\lambda_1 \lambda_2}}\right) \tag{3}$$

where λ_i denote the eigenvalues of the fiber orientation tensor, ordered in ascending magnitude.

Table 2. Observed Hellinger distances between dual-SPIM and quad-SPIM acquisition for five selected ROIs.

ROI id	Observed Hellinger Distance H (P, Q)
1	0.099
2	0.139
3	0.137
4	0.065
5	0.130

For comparative analysis, N = 5 distinct square regions of interest (ROIs), each measuring 1 mm^2, were selected from both dual-SPIM and quad-SPIM acquisitions. The empirical distributions of local ODI values were computed using a spatial sampling step of 100 µm, corresponding to cubic super-voxels with 100 µm sides (Figure 4e–g). As a result, N = 100 ODI values for each ROI were extracted and were first visualized by plotting histograms - using the Freedman-Diaconis rule to determine the optimal number of bins – overlaid with Gaussian Kernel Density Estimates (KDE) (Figure 4h).

The Hellinger distances calculated for the 5 ROIs between dual-SPIM and quad-SPIM are listed in **Table 2**.

The observed distances (listed in Table 2) are below an equivalence threshold of $\epsilon = 0.15$, suggesting a high overall similarity. This can be quantified thanks to the Bhattacharyya coefficient, defined as:

$$B\left(P, Q\right) = \sum_{x} \sqrt{P\left(x\right) Q\left(x\right)} \tag{4}$$

which assesses the overlap between two probability distributions *P and Q*, and it measures 1 when the distributions are identical and 0 when they are completely disjoint. Since the Hellinger distance $H(P, Q)$ is related to $B(P, Q)$ through the equation:

$$H\left(P, Q\right) = 1 - B\left(P, Q\right)^2 \tag{5}$$

Low values of $H(P, Q)$ are reflected into high overlaps between the distribution functions and, in the specific case described here, the threshold value of distances of 0.15 implies a 97.75% overlap between the two acquisition setups.

To formally test whether these observed distances reflect true equivalence between the distributions rather than random similarity, a nonparametric bootstrap equivalence test was performed (see the Experimental Section for further details). The goal of the test is to show that the true Hellinger distance H(P, Q) does not exceed a tolerance value ϵ.[43,44]

Table 3 reports the values of the Hellinger distances of each ROI calculated through bootstrap distribution estimates and the corresponding 95% confidence intervals (CI upper).

This outcome highlights an important feature of the test: it evaluates not only the central tendency, but also the reliability of the observed similarity. The bootstrap procedure reflects how the Hellinger distance might vary if data collection were repeated. As a result, the upper bounds of the confidence interval may exceed a fixed ϵ, leading to conservative decisions. In this sense, the test penalizes variability to ensure that the conclusions remain robust under sampling uncertainty. To address this, we adopt a data-driven approach: ϵ is set empirically as the 95th percentile of the bootstrap distribution of Hellinger distances. This means choosing the smallest ϵ such that 95% of the resampled distances remain below it – a conservative yet adaptive threshold. In our case, this value corresponds to $\epsilon = 0.25$, which translates to an overlap of ≈93.75%, according to the Bhattacharyya coefficient. At this threshold, all ROIs meet the equivalence criterion, including both the observed distances and their upper confidence interval bounds.

Table 3. Measured Hellinger bootstrap distributions and the corresponding upper bound of the 95% confidence interval for each ROI. The last column highlights that all the ROIs tested and acquired with different setups meet the equivalence criterion at the threshold of $\epsilon = 0.25$.

ROI id	Bootstrap Hellinger Distance	CI upper [95%]	Equivalence [<0.25]
1	0.099	0.178	Yes
2	0.138	0.223	Yes
3	0.136	0.221	Yes
4	0.065	0.155	Yes
5	0.130	0.210	Yes

In summary, the empirical distributions of local dispersion between dSPIM and qSPIM acquisitions are nearly identical across all ROIs. When accounting for sampling uncertainty via bootstrap, this similarity holds robustly under a data-driven tolerance of $\epsilon = 0.25$. Thus, statistical equivalence between dSPIM and qSPIM measurements on the analyzed scale can be reliably concluded.

3. Conclusion

In this study, we introduced a novel quad-SPIM microscope, representing a substantial advancement in light-sheet fluorescence microscopy. The system offers significant improvements in imaging speed and multiplexing and multicolor capabilities, establishing it as a powerful tool for large-scale imaging of human brain samples while preserving single-cell resolution.

The most notable enhancement is an 11-fold increase in the acquisition speed compared to the dual-SPIM configuration previously in use. The quad-SPIM achieves a volumetric imaging rate of 3.2 $cm^3\ h^{-1}$ across four fluorescence channels, a dramatic improvement over the prior speed of 0.29 $cm^3\ h^{-1}$. The gain is especially critical for high-resolution imaging of large and complex brain specimens, significantly reducing acquisition times while maintaining high spatial resolution. Such performance makes the system well-suited for large-scale studies, including neural circuit mapping and investigations into neurodegenerative conditions.

The system's ability to acquire four-color data simultaneously greatly enhances its flexibility, enabling multiplexed imaging of various biomarkers within the same sample. This is particularly advantageous for studying complex biological processes, such as neuronal connectivity and cell-type-specific interactions. With lateral resolution ranging from 2.1 to 2.7 µm and adequate axial resolution, the system supports single-cell imaging even in relatively thick specimens, offering valuable insights into brain structure at both cellular and subcellular levels.

The quad-SPIM has also demonstrated its utility in specific biological applications, including the quantification of fiber orientation dispersion at the spatial scale of 100 µm in brain tissue using tools such as the Foa3D software. The equivalence bootstrap test performed has confirmed the comparable performances, at the chosen resolution scale, of the newly built microscope with those of the setup used by our group in the past years. These use cases underscore the microscope's potential to contribute to critical questions in neuroscience.

In synthesis, while the resolution of the current quad-SPIM configuration is moderate due to the use of a 5×/0.15 NA objective, this design choice enables the system to achieve high-speed, four-channel multiplexed imaging of large, cleared human brain samples. The objective provides a favorable balance between field of view, working distance, and compatibility with high-refractive-index immersion media, allowing efficient imaging across centimeter-scale volumes at cellular resolution. Despite the moderate NA, the system supports robust quantification of axonal orientation using DiD staining, with orientation dispersion metrics statistically equivalent to those obtained using a higher-resolution dual-SPIM configuration in use in our labs, as validated through the Foa3D pipeline and equivalence testing. These results demonstrate the suitability of the quad-SPIM for high-throughput, multiplexed structural mapping of complex tissues. Future developments will include the integration of custom-built objectives with higher numerical aperture and extended working distance to improve spatial resolution, which could enable the system to approach single-axon resolution, and to potentially adopt a more classical, symmetric 45° dual-objective geometries. Moreover, future implementations will also integrate LSFM microscopy within our quad-SPIM system in combination with expansion microscopy techniques. By applying anisotropic sample expansion of four to tenfold, and leveraging the high acquisition speed of the quad-SPIM setup, this approach would enable substantially improved resolution when imaging expanded samples, while still maintaining reasonable acquisition times.

Looking ahead, the quad-SPIM system holds strong promise for both fundamental and translational research. Its speed and multiplexing capabilities make it ideal for generating cellular-resolution brain atlases and for exploring neurodevelopmental dynamics and degenerative processes. These features could support the development of new diagnostic and therapeutic strategies.

Future enhancements may include the integration of additional laser lines and further optimization of the light-sheet and detection optics to improve resolution and penetration depth. Coupled with advancements in sample preparation and data processing, the quad-SPIM could become a central platform across multiple disciplines, including oncology, developmental biology, and regenerative medicine.

4. Experimental Section

Beads for PSF Evaluation: For a correct measurement of the system's PSF, sub-diffraction-sized fluorescent beads were used as point light sources. The 500-nm-diameter fluorescent spheres (TetraSpeck, Invitrogen) were diluted 1:1000 v/v in the imaging buffer medium (91% glycerol v/v, RI = 1.46). The obtained solution containing the fluorescent beads was mounted between a square glass microscope slide and a quartz coverslip. The two slides were glued together with adhesive tape. The sample was then placed in the imaging chamber, where it was illuminated with the four laser lines. Images were acquired in the four channels with a 730 nm step size along the *x*-axis, corresponding to a 250 nm increment along the optical axis of the detection objective. After acquisition, images were re-oriented on the sample plane through a deskewing process. Therefore, in the acquired images, the effective pixel size on the *x* and *y* axes coincides with the nominal one of 1.3 µm, whereas its dimension on the *z*-axis is 0.25 µm.

Human Samples: The human brain samples used in this work were obtained from control subjects who died of natural causes with no clinical diagnoses or neuropathology. A standard fixation protocol was used in which the brain was fixed in 10% formalin for a minimum of 90 days. Brainstem and Broca's area samples were provided by the Department of Neuropathology at the Massachusetts General Hospital Autopsy Service (Boston, USA). Written consent was obtained from healthy participants before death, following institutional review board–approved tissue collection protocols from Partners Institutional Biosafety Committee (protocol 2003P001937). Tissue sections were stored at 4 °C in PBS 0.02% NaN_3.

Human Samples—Broca's Area Tissue Preparation: Human brain slices (500 µm or 1 mm thick) from Broca's area were processed as previously described in a previous work by our group[25] by using the SHORT method,[40] a modified SWITCH/TDE tissue transformation protocol[26] that combines the SWITCH technique[18,45] with the TDE clearing method.[46,47] Slices were first incubated in a low-pH SWITCH-off buffer (50% Phosphate-Buffered saline (PBS) titrated to pH 3 using HCl, 25% 0.1 M HCl, 25% 0.1 M potassium hydrogen phthalate, and 4% glutaraldehyde) for 24 h at 4 °C, and then they were placed in a SWITCH-off buffer (PBS (pH 7.4) with 1% glutaraldehyde) and the incubation was performed at 4 °C for 24 h. After three PBS washes (2 h each, RT), samples were inactivated by overnight incubation at 37 °C in 1× PBS (pH 7.4), 4% w/v acetamide, 4% w/v glycine, pH 9.0 solution. After three PBS washes (2 h each, RT), they were incubated for 6 days at 55 °C in the clearing solution (200 mM sodium dodecyl sulphate (SDS), 20 mM sodium sulphite (Na_2SO_3), and 20 mM boric acid (H_3BO_3), pH 9.0). Post-clearing, tissues were washed in PBST (PBS + 0.1% Triton X-100) for 24 h at 37 °C. To reduce autofluorescence from lipofuscin and free aldehydes, samples were treated with hydrogen peroxide (30%, v/v) for 45–90 min at room temperature (RT) and then washed in PBS (three washes, 15 min each, RT). Antigen retrieval was performed using preheated (95 °C) Tris-EDTA buffer pH 9 (10 mM tris base v/v, 1 mM EDTA solution w/v, and 0.05% Tween 20 v/v) for 10 min, followed by cooling down at RT and equilibration with PBS for 1 h. The specimens were then incubated with primary antibodies diluted in PBST with 0.01% w/v NaN3, at 37 °C with gentle shaking for 7 days. The primary antibodies used are: anti-NeuN antibody (Merck Life Science, #ABN91; RRID:AB 11 205 760), diluted 1:50; anti-tyrosine hydroxylase (Merck Life Science, #AB152; RRID:AB 390 204), diluted 1:500; anti-somatostatin (Santa Cruz Biotechnology, #sc.47706; RRID:AB 628 268) diluted 1:200; and anti-calretinin (Protein-Tech, 12278-1-A; RRID:AB 2 228 338) diluted 1:200. After washing with PBST at 37 °C for 24 h, samples were incubated for 5 days at 37 °C with the secondary antibodies conjugated with different Alexa Fluor dyes diluted 1:200 in PBST with 0.01% w/v NaN3 at 37 °C. The secondary antibodies used are: Goat anti-Chicken IgY (H+L) Alexa Fluor 647 (Invitrogen, #ab150171, RRID:AB 2 921 318); Goat anti-Rabbit IgG (H&L) Alexa Fluor 568 (Abcam, #ab175471, RRID:AB 2 576 207); Donkey Anti-Rat IgG (H&L) Alexa Fluor 568 (Abcam,m#ab175475, RRID:AB 2 636 887); Alpaca Anti-Rabbit IgG (H&L) Alexa Fluor 488 (Jackson ImmunoResearch Labs; #611-545-215, RRID:AB 2 721 874), followed by three 2-h washes with PBST at 37 °C. To achieve optical transparency, samples were soaked first in a solution with 30% TDE/PBS (v/v), then in 68% TDE/PBS (v/v) (each for 2 h, RT, with gentle shaking). The slices were mounted between a 250 µm-thick quartz coverslip and a standard glass slide with a 500 µm steel spacer in between.[47] The imaging medium is a solution of 91% glycerol in distilled water to match the refractive index of the brain samples and minimize optical aberrations during LSFM acquisition.

Human Samples—Brainstem Tissue Preparation: The human brainstem slab (300 µm thick) was processed using the same SHORT protocol described for Broca's area slices. Following the clearing protocol, myelinated fibers were stained as previously described in ref. [42] For fiber staining, the lipophilic dye DiD (Invitrogen, #D7757) was used. A 3 mg mL^{-1} stock solution was prepared by dissolving lyophilized DiD in 10% SDS in 1X PBS and stored at room temperature. The tissue slab was pre-equilibrated overnight at 37 °C in 10 mM SDS in 1X PBS with gentle shaking. It was then incubated in a *D-off* solution (0.025 mg mL^{-1} DiD in 10 mM SDS in 1X PBS) for 24 h at 37 °C, followed by 24 h in a *D-on* solution (0.025 mg mL^{-1} DiD in 1X PBS with 0.1% Triton X-100) under the same conditions. Unbound dye was removed by washing the tissue in 1X PBST for 24 h at 37 °C with gentle shaking. To achieve optical transparency, samples were soaked first in a solution with 30% TDE/PBS (v/v), then in 68% TDE/PBS (v/v). The slab was placed in a glass-quartz sandwich with a 300 µm-thick spacer, filled with 68% TDE/PBS (v/v). The final refractive index matching was performed with 91% glycerol as the imaging buffer as described above.

Control Software: The microscope is operated via two dedicated workstations running a custom software developed in-house, originally for previous systems and now adapted to the current LSFM setup. This open-source platform, called *SpimLAB* (https://github.com/lens-biophotonics/SPIMlab), is written in C++ using Qt libraries and comprises approximately 10 000 lines of code. *SpimLAB* manages hardware synchronization and triggering through a National Instruments PCIe-6363 multifunction I/O board, enabling automated, high-speed image acquisition from four sCMOS cameras in confocal detection mode, with data streamed at nearly 1GB/s per pair of cameras and saved directly to an SSD volume. The acquisition process begins by finding the sample boundaries both in the *x* and *y* directions. Image stacks are captured as the sample moves along the x-axis through the fixed FOV of the detection objective. After each stack, the sample shifts by 2.4 mm along the y-axis, repeating the process until the entire volume is covered. A 200 µm overlap between adjacent stacks is maintained to facilitate post-processing alignment, with metadata saved alongside each stack. The software allows fine control of the camera parameters and galvo mirrors to synchronize the rolling shutter of the cameras with the scanned light sheets. Users can select active imaging channels and configure laser lines via AOTF settings. The software, originally developed for our dual-view light-sheet setup, was adapted to the new microscope as follows. A workstation acts as the main computer, directly controlling two cameras (via two frame grabbers) and the multifunction I/O board for signal generation. A second workstation controls two more cameras and receives commands from the main workstation through the LAN (Local Area Network).

Image Processing: During acquisition, raw data are saved in multi-tiff files, and the scanning coordinates are saved in associated files containing the information needed for a correct image reconstruction. Images contained in the raw data are oriented as the detection objective focal plane, which is tilted by 20 degrees with respect to the sample plane. For this reason, to obtain a correct stitching and a 3D image reconstruction, images have to be re-oriented on the sample plane. This is done by means of a deskewing process, which consists of a re-assignment of the pixels' position through affine transformations, including rotations. After that, the lateral voxel size is resampled to match the axial voxel size in order to obtain an isotropic voxel in the 3D reconstruction of the image. Finally, image stitching is performed on each horizontal scanning line, and horizontal lines are then stitched by overlapping each other by 10% along the y-axis. The resulting file is a multi-page TIFF z-stack where all the frames are aligned with the sample plane. All of these operations are performed through an open-source software-previously developed by our group[39,48]- called *Zetastitcher* (https://github.com/lens-biophotonics/ZetaStitcher/), capable of stitching files composed of 10^{12} voxels. For visualization purposes only, stripe artifact correction was applied to the stitched MIP images to mitigate horizontal illumination inhomogeneities introduced during image acquisition. A smoothed illumination field was estimated using a directionally biased Gaussian filter, designed to capture broad intensity variations along the axis perpendicular to the stripes. The original image was then normalized by this background, reducing stripe artifacts and improving visual uniformity while preserving structural detail.

Nonparametric Bootstrap Equivalence Test: In order to quantify the similarity between fiber orientation dispersion distributions, the Hellinger distance function H(P,Q), defined in Equation (6), was used in its continuous form:

$$H(P,Q) = \frac{1}{\sqrt{2}}\left(\int \left(\sqrt{p(x)} - \sqrt{q(x)} \right)^2 dx \right)^{\frac{1}{2}} \quad (6)$$

$H(P, Q)$ is symmetric, non-negative, and ranges between 0 (identical distributions) and 1 (non-overlapping distributions), given that $p(x)$ and $q(x)$ are two absolutely continuous probability density functions.

Unlike classical difference testing, which aims to detect any significant deviation, equivalence testing seeks evidence supporting the absence of a meaningful difference, thus requiring a different inferential framework. Accordingly, the hypothesis system is:

- H_0 (null hypothesis): the two distributions are not equivalent, thus the Hellinger distance between the two is higher than ϵ;
- H_1 (alternative hypothesis): the two distributions are equivalent, thus the Hellinger distance between the two is lower than or equal to ϵ.

The nonparametric bootstrap equivalence test then proceeds as follows:

- Bootstrap sampling: from each pair of ROIs, dispersion values are resampled with replacement. KDE is applied to each replicate to compute the Hellinger distance H_b*.
- Confidence interval: the one-sided 95% upper confidence bound (CI upper) is computed by taking the $(1-\alpha)$- quantile (with $\alpha = 0.05$) of the bootstrap distribution {Hb*} with b = 1, 2, ..., 2000.
- Decision rule: reject H_0 (i.e., accept equivalence) if both the observed Hellinger distance and its upper confidence bound lie below ϵ.

This two-part criterion ensures that the inferred similarity remains valid even under resampling variability. It is intentionally conservative, as equivalence is only accepted when there is strong evidence that the true distance lies below ϵ with high confidence.

Supporting Information

Supporting Information is available from the Wiley Online Library or from the author.

Acknowledgements

The authors express their gratitude to the donor involved in the body donation program of the Massachusetts General Hospital Autopsy Service, USA, who made this study possible by generously donating their body to science. This project has received funding from the European Union's Horizon Europe research and innovation programme under Grant agreement No. 101147319 (EBRAINS 2.0) and under Grant agreement No. 654148 (Laserlab-Europe). This research has also been supported by the Italian Ministry for University and Research in the framework of the Advanced Light Microscopy Italian Node of Euro-Bioimaging ERIC, from the General Hospital Corporation Centre of the National Institutes of Health under award number U01 MH117023, and BRAIN CONNECTS (award number U01 NS132181). The content of this work is solely the responsibility of the authors and does not necessarily represent the official views of the National Institutes of Health-USA. The work was also supported by Fondazione Cassa di Risparmio di Firenze (Human Brain Optical Mapping project). Additional funding was provided by the University of Florence (D.R. no. 464 del 02/04/2024) for the project "Smart hy-

drogels with enhanced toughness to enable human brain tissue clearing (SMART-brain)," CUP: B97G24000240005 and by RICTD2025_2026-CUP: B97G24000240005, by LENS and CNR for the technical and scientific support to the Italian National Node FOE 2022 - CUP B53C24004790001.

Open access publishing facilitated by Universita degli Studi di Firenze, as part of the Wiley - CRUI-CARE agreement.

Conflict of Interest

The authors declare no conflict of interest.

Data Availability Statement

The datasets generated and analyzed during the current study are available from the corresponding author on reasonable request.

Keywords

connectomics, high-speed volumetric imaging, image processing, light-sheet microscopy, multiplexing, neuroanatomy, neuropathology

Received: July 3, 2025
Revised: August 28, 2025
Published online:

[1] J. R. Swedlow, K. Hu, P. D. Andrews, D. S. Roos, J. M. Murray, *Proceedings of the National Academy of Sciences*, **2002**, *99*, 2014.
[2] J. R. Swedlow, *BioEssays* **2012**, *34*, 333.
[3] P. D. Andrews, I. S. Harper, J. R. Swedlow, *Traffic* **2002**, *3*, 29.
[4] M. Sergides, L. Perego, T. Galgani, C. Arbore, F. S. Pavone, M. Capitanio, *The European Physical Journal Plus* **2021**, *136*, 316.
[5] L. Perego, C. Dallari, C. Falciani, A. Pini, L. Gardini, C. Credi, F. S. Pavone, *Journal of Biophotonics* **2025**, *18*, 202400519.
[6] R. Wolleschensky, B. Zimmermann, M. Kempe, *J. Biomed. Opt.* **2006**, *11*, 064011.
[7] W. J. Alford, R. D. VanderNeut, V. J. Zaleckas, *Proceedings of the IEEE*, **1982**, *70*, pp. 641–651.
[8] A. Diaspro, G. Chirico, C. Usai, P. Ramoino, J. Dobrucki, "*Handbook of Biological Confocal Microscopy*," (Ed.: J. B. Pawley), Springer US, Boston, MA, **2006**, pp. 690–702.
[9] O. E. Olarte, J. Andilla, E. J. Gualda, P. Loza-Alvarez, *Adv. Opt. Photonics* **2018**, *10*, 111.
[10] E. H. K. Stelzer, F. Strobl, B.o-J. Chang, F. Preusser, S. Preibisch, K. McDole, R. Fiolka, *Nature Reviews Methods Primers* **2021**, *1*, 73.
[11] P. A. Santi, *J. Histochem. Cytochem.* **2011**, *59*, 129.
[12] B.i-C. Chen, W. R. Legant, K. Wang, L. Shao, D. E. Milkie, M. W. Davidson, C. Janetopoulos, X. S. Wu, J. A. Hammer, Z. Liu, B. P. English, Y. Mimori-Kiyosue, D. P. Romero, A. T. Ritter, J. Lippincott-Schwartz, L. Fritz-Laylin, R. D. Mullins, D. M. Mitchell, J. N. Bembenek, A.-C. Reymann, R. Böhme, S. W. Grill, J. T. Wang, G. Seydoux, U. S. Tulu, D. P. Kiehart, E. Betzig, *Science* **2014**, *346*, 1257998.
[13] K. McDole, L. Guignard, F. Amat, A. Berger, G. Malandain, L. A. Royer, S. C. Turaga, K. Branson, P. J. Keller, *Cell* **2018**, *175*, 859.
[14] P. K. Poola, M. I. Afzal, Y. Yoo, K. H. Kim, E. Chung, *Biomed. Eng. Lett.* **2019**, *9*, 279.
[15] M. B. Ahrens, M. B. Orger, D. N. Robson, J. M. Li, P. J. Keller, *Nat. Methods* **2013**, *10*, 413.
[16] R. M. Power, J. Huisken, *Nat. Methods* **2017**, *14*, 360.
[17] P. Spangenberg, N. Hagemann, A. Squire, N. Förster, S. D. Krauß, Y. Qi, A. Mohamud Yusuf, J. Wang, A. Grüneboom, L. Kowitz, S. Korste, M. Totzeck, Z. Cibir, A. A. Tuz, V. Singh, D. Siemes, L. Struensee, D. R. Engel, P. Ludewig, L. Martins Nascentes Melo, I. Helfrich, J. Chen, M. Gunzer, D. M. Hermann, A. Mosig, *Cell Reports Methods* **2023**, *3*, 100436.
[18] D. Di Meo, J. Ramazzotti, M. Scardigli, F. Cheli, L. Pesce, N. Brady, G. Mazzamuto, I. Costantini, F. S. Pavone, *Journal of Visualized Experiments* **2024**, https://doi.org/10.3791/65960.
[19] M. Pawłowska, D. Legutko, M. Stefaniuk, *Postepy biochemii* **2017**, *63*, 8.
[20] S. Corsetti, F. Gunn-Moore, K. Dholakia, *J. Neurosci. Methods* **2019**, *319*, 16.
[21] I. Costantini, G. Mazzamuto, M. Roffilli, A. Laurino, F. Maria Castelli, M. Neri, G. Lughi, A. Simonetto, E. Lazzeri, L. Pesce, C. Destrieux, L. Silvestri, V. Conti, R. Guerrini, F. Saverio Pavone, *Biomed. Opt. Express* **2021**, *12*, 3684.
[22] I. Costantini, L. Morgan, J. Yang, Y. Balbastre, D. Varadarajan, L. Pesce, M. Scardigli, G. Mazzamuto, V. Gavryusev, F. M. Castelli, M. Roffilli, L. Silvestri, J. Laffey, S. Raia, M. Varghese, B. Wicinski, S. Chang, I. A. Chen, H. Wang, D. Cordero, M. Vera, J. Nolan, K. Nestor, J. Mora, J. E. Iglesias, E. Garcia Pallares, K. Evancic, J. C. Augustinack, M. Fogarty, A. V. Dalca, et al., *Sci. Adv.* **2023**, *9*, https://doi.org/10.1126/sciadv.adg3844.
[23] H. R. Ueda, A. Ertürk, K. Chung, V. Gradinaru, A. Chédotal, P. Tomancak, P. J. Keller, *Nat. Rev. Neurosci.* **2020**, *21*, 61
[24] H.-U. Dodt, U. Leischner, A. Schierloh, N. Jährling, C. P. Mauch, K. Deininger, J. M. Deussing, M. Eder, W. Zieglgänsberger, K. Becker, *Nat. Methods* **2007**, *4*, 331.
[25] D. D. Meo, M. Sorelli, J. Ramazzotti, F. Cheli, S. Bradley, L. Perego, B. Lorenzon, G. Mazzamuto, A. Emmi, A. Porzionato, R. De Caro, *bioRxiv* **2024**, https://doi.org/10.1101/2024.09.10.612232.
[26] I. Costantini, R. Cicchi, L. Silvestri, F. Vanzi, F. S. Pavone, *Biomed. Opt. Express* **2019**, *10*, 5251.
[27] L. Silvestri, I. Costantini, L. Sacconi, F. S. Pavone, *J. Biomed. Opt.* **2016**, *21*, 081205.
[28] C. Olianti, F. Giardini, E. Lazzeri, I. Costantini, L. Silvestri, R. Coppini, E. Cerbai, F. S. Pavone, L. Sacconi, *Progress in Biophysics and Molecular Biology* **2022**, *168*, 10.
[29] E. G. Reynaud, U. Krzic, K. Greger, E. H. K. Stelzer, *HFSP Journal* **2008**, *2*, 266.
[30] G. A. Johnson, Y. Tian, D. G. Ashbrook, G. P. Cofer, J. J. Cook, J. C. Gee, A. Hall, K. Hornburg, C. C. Kaczorowski, Y.i Qi, F.-C. Yeh, N. Wang, L. E. White, R. W. Williams, *Proceedings of the National Academy of Sciences* **2023**, *120*, 2218617120.
[31] J. Yang, I. A. Chen, S. Chang, J. Tang, B. Lee, K. Kili, S. Sunil, H. Wang, D. Varadarajan, C. Magnain, S.-C. Chen, I. Costantini, F. Pavone, B. Fischl, D. A. Boas, *Neurophotonics* **2020**, *7*, 045005.
[32] M. Menzel, M. Axer, H. De Raedt, I. Costantini, L. Silvestri, F. S. Pavone, K. Amunts, K. Michielsen, *Phys. Rev. X* **2020**, *10*, 021002.
[33] M. C. Müllenbroich, L. Turrini, L. Silvestri, T. Alterini, A. Gheisari, N. Tiso, F. Vanzi, L. Sacconi, F. S. Pavone, *Frontiers in Cellular Neuroscience* **2018**, *12*, 315.
[34] L. Silvestri, A. Bria, L. Sacconi, G. Iannello, F. S. Pavone, *Opt. Express* **2012**, *20*, 20582.
[35] E. M. C. Hillman, V. Voleti, W. Li, H. Yu, *Annu. Rev. Neurosci.* **2019**, *42*, 295.
[36] C. M. Hobson, M. Guo, H. D. Vishwasrao, Y. Wu, H. Shroff, T.-L. Chew, *Nat. Methods* **2022**, *19*, 1538
[37] B. Chen, B.o-J. Chang, P. Roudot, F. Zhou, E. Sapoznik, M. Marlar-Pavey, J. B. Hayes, P. T. Brown, C.-W. Zeng, T. Lambert, J. R. Friedman, C.-L.i Zhang, D. T. Burnette, D. P. Shepherd, K. M. Dean, R. P. Fiolka, *Nat. Methods* **2022**, *19*, 1419.
[38] S. Daetwyler, R. P. Fiolka, *Commun. Biol.* **2023**, *6*, 502.

[39] G. Mazzamuto, L. Silvestri, G. Sancataldo, V. Gavryusev, M. Scardigli, I. Costantini, F. S. Pavone, *Three-Dimensional and Multidimensional Microscopy: Image Acquisition and Processing XXX*. **2023**, *12385*, 10.
[40] L. Pesce, M. Scardigli, V. Gavryusev, A. Laurino, G. Mazzamuto, N. Brady, G. Sancataldo, L. Silvestri, C. Destrieux, P. R. Hof, I. Costantini, F. S. Pavone, *Commun. Biol.* **2022**, *5*, 447.
[41] M. Sorelli, I. Costantini, L. Bocchi, M. Axer, F. S. Pavone, G. Mazzamuto, *Sci. Rep.* **2023**, *13*, 4160.
[42] M. Sorelli, D. Di Meo, S. Bradley, F. Cheli, J. Ramazzotti, L. Perego, C. Destrieux, P. R. Hof, F. S. Pavone, G. Mazzamuto, I. Costantini, *bioRxiv* **2025**, 2025.
[43] D. Lakens, *Soc. Psychol. Pers. Sci.* **2017**, *8*, 355.
[44] G. James, D. Witten, T. Hastie, R. Tibshirani, *An Introduction to Statistical Learning*, Springer, New York, NY, **2013**.
[45] E. Murray, J. H. Cho, D. Goodwin, T. Ku, J. Swaney, S.-Y. Kim, H. Choi, Y.-G. Park, J.-Y. Park, A. Hubbert, M. McCue, S. Vassallo, N. Bakh, M. P. Frosch, V. J. Wedeen, H. S. Seung, K. Chung, *Cell* **2015**, *163*, 1500.
[46] I. Costantini, J.-P. Ghobril, A. P. Di Giovanna, A. L. A. Mascaro, L. Silvestri, M. C. Müllenbroich, L. Onofri, V. Conti, F. Vanzi, L. Sacconi, R. Guerrini, H. Markram, G. Iannello, F. S. Pavone, *Sci. Rep.* **2015**, *5*, 9808.
[47] M. Scardigli, L. Pesce, N. Brady, G. Mazzamuto, V. Gavryusev, L. Silvestri, P. R. Hof, C. Destrieux, I. Costantini, F. S. Pavone, *Frontiers in Neuroanatomy* **2021**, *15*, 752234.
[48] G. Mazzamuto, L. Silvestri, I. Costantini, F. Orsini, M. Roffilli, P. Frasconi, L. Sacconi, F. S. Pavone, *Biophotonics Congress: Biomedical Optics Congress 2018 (Microscopy/Translational/Brain/OTS) (2018), paper JTh3A.64*. **2018**, https://doi.org/10.1364/TRANSLATIONAL.2018.JTh3A.64.